The origin of physical variations in the star formation law

Christoph Federrath[1] $\star$

[1]*Monash Centre for Astrophysics, School of Mathematical Sciences, Monash University, VIC 3800, Australia*

12 December 2013

ABSTRACT
Observations of external galaxies and of local star-forming clouds in the Milky Way have suggested a variety of star formation laws, i.e. simple direct relations between the column density of star formation (Σ_{SFR}: the amount of gas forming stars per unit area and time) and the column density of available gas (Σ_{gas}). Extending previous studies, we show that these different, sometimes contradictory relations for Milky Way clouds, nearby galaxies, and high-redshift discs and starbursts can be combined in one universal star formation law in which Σ_{SFR} is about 1% of the local gas collapse rate, $\Sigma_{\mathrm{gas}}/t_{\mathrm{ff}}$, but a significant scatter remains in this relation. Using computer simulations and theoretical models, we find that the observed scatter may be primarily controlled by physical variations in the Mach number of the turbulence and by differences in the star formation efficiency. Secondary variations can be induced by changes in the virial parameter, turbulent driving and magnetic field. The predictions of our models are testable with observations that constrain both the Mach number and the star formation efficiency in Milky Way clouds, external disc and starburst galaxies at low and high redshift. We also find that reduced telescope resolution does not strongly affect such measurements when Σ_{SFR} is plotted against $\Sigma_{\mathrm{gas}}/t_{\mathrm{ff}}$.

Key words: galaxies: turbulence – stars: formation – ISM: clouds – galaxies: high-redshift – galaxies: ISM – galaxies: starburst.

1   INTRODUCTION

Stars form in dense molecular cores inside giant molecular clouds in the interstellar medium (Ferrière 2001). These clouds are highly turbulent and magnetized, and are in approximate virial equilibrium with comparable values of the gravitational, kinetic and magnetic energy (Stahler & Palla 2004). Despite continuous efforts over the last decades, we still do not know which physical processes determine the star formation rate (SFR) in our Galaxy and in extragalactic systems, such as disc and starburst galaxies. We do know, however, that turbulence plays a key role in controlling the star formation process (Mac Low & Klessen 2004; Elmegreen & Scalo 2004; McKee & Ostriker 2007). Almost all of our current knowledge about star formation comes from submillimetre observations. These observations provide us with maps of gas or dust column density (Σ_{gas}), which can be combined with young stellar object (YSO) counts, infrared, or ultraviolet luminosities, to yield the column density of star formation (Σ_{SFR}). Such data have been collected for nearby and distant galaxies, and for clouds in the Milky Way (MW).

Figure 1 shows a plot of Σ_{SFR} versus Σ_{gas}, combining the most recent measurements in MW clouds, as well

as nearby and high-redshift disc and starburst galaxies. For comparison, four previously suggested star formation laws are shown with different line styles. First of all, we see that most of the MW data lie systematically above the extragalactic relations (Kennicutt 1998; Bigiel et al. 2008) by about an order of magnitude in Σ_{SFR}. Secondly, for any given Σ_{gas}, we see a large range of Σ_{SFR}, spanning about two orders of magnitude or more. Thirdly, the Lada et al. (2010, hereafter L10) clouds, measured at an extinction threshold of $A_{\mathrm{K}} \geqslant 0.8\,\mathrm{mag}$ (filled circles) are systematically higher in both Σ_{gas} and Σ_{SFR} than *the same clouds* evaluated for $A_{\mathrm{K}} \geqslant 0.1\,\mathrm{mag}$ (open circles). Given the broad distribution of observational data in Figure 1, a universal star formation law seems quite elusive. Although the overall correlation between Σ_{SFR} and Σ_{gas} suggests that denser gas forms stars at a higher rate, the scatter is significant and there appears to be a bimodal distribution between disc and starburst galaxies.

Recently, Heiderman et al. (2010, hereafter H10) explained the systematic elevation of MW clouds over extragalactic systems by the fact that observations of star formation in MW clouds resolve individual sites of star formation, while observations of distant galaxies inevitably average over large areas, because of the limited telescope resolution. This alone, however, does not explain the bimodal distribution between disc and starburst galaxies seen in Figure 1.

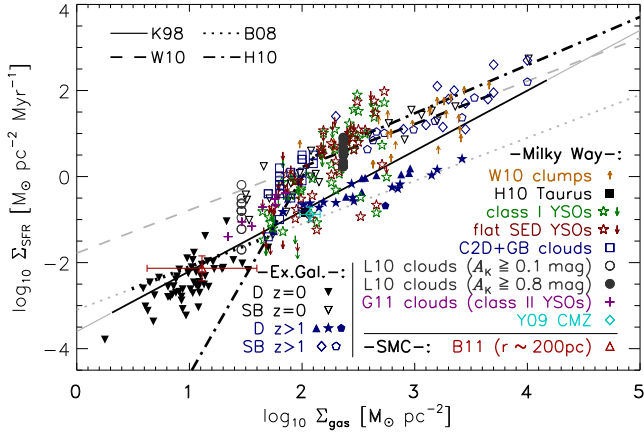$\star$ E-mail: christoph.federrath@monash.edu

Figure 1. Star formation rate column density (Σ_{SFR}) versus gas column density (Σ_{gas}), measured in MW clouds, as well as in nearby and high-redshift disc and starburst galaxies. The data shown are from W10 (Wu et al. 2010): HCN(1–0) clumps (uparrows); from H10 (Heiderman et al. 2010): Taurus (filled square), class I YSOs and flat SED YSOs (green and red stars with upper limits shown as downarrows), and C2D+GB clouds (open squares); from L10 (Lada et al. 2010): molecular clouds observed at two different extinction thresholds ($A_{\mathrm{K}} \geqslant 0.1$ mag: open circles, and $A_{\mathrm{K}} \geqslant 0.8$ mag: filled circles); from G11 (Gutermuth et al. 2011): class II YSO counts in eight molecular clouds (crosses); from Y09 (Yusef-Zadeh et al. 2009): the Central Molecular Zone (CMZ, turquoise diamond with error bars); and from B11 (Bolatto et al. 2011): the Small Magellanic Cloud (SMC, red triangle with error bars). Extragalactic data (Kennicutt 1998; Bouché et al. 2007; Daddi et al. 2010; Genzel et al. 2010; Tacconi et al. 2010) of disc (D) and starburst (SB) galaxies at low redshift ($z = 0$) and high redshift ($z \sim 1$–3) are reproduced from the tabulated compilation in KDM12 (Krumholz et al. 2012). (Table 3 in KDM12 for Ds and SBs contains naming errors and SB galaxy VII Zw 31, erroneously called 'NGC 7552', has wrong Σ_{gas} and Σ_{SFR}. An erratum is in preparation [M. Krumholz, private communication] and those errors have been corrected here.) Typical uncertainties for the Ds and SBs are of the order of 0.5 dex (factor of 3) in both Σ_{gas} and Σ_{SFR} (Kennicutt 1998), but there may be additional uncertainties due to calibration errors caused by different forms of the initial mass function and different CO/H_2 conversion factors (Daddi et al. 2010). Previously suggested star formation laws from extragalactic observations by K98 (Kennicutt 1998) and B08 (Bigiel et al. 2008), as well as from MW observations by W10 and H10 are shown as lines for comparison.

2   A MORE UNIVERSAL STAR FORMATION LAW

More recently, Krumholz et al. (2012, hereafter KDM12) thus argued that the standard star formation relation shown in Figure 1 may not provide the best physical representation. Based on the assumption that the SFR is inversely proportional to the dynamical time of the gas (Schmidt 1959; Elmegreen 2002), KDM12 suggest that a better fit is obtained, if Σ_{SFR} is plotted against $\Sigma_{\mathrm{gas}}/t_{\mathrm{ff}}$, i.e. Σ_{SFR} as a function of Σ_{gas} divided by the local gas collapse time,

$$t_{\mathrm{ff}}(\rho) = \left(\frac{3\pi}{32\,G\rho} \right)^{1/2}, \qquad (1)$$

evaluated for each cloud or galactic system individually. Although not directly observable, the gas density $\rho = (3\sqrt{\pi}/4)M/A^{3/2}$ with the cloud mass $M = \Sigma_{\mathrm{gas}}A$ and

the observed area A can be estimated by assuming that the clouds are approximately spherical objects (KDM12), introducing additional uncertainties (Appendix A). For extragalactic systems, the gas collapse time is taken to be the minimum of the Toomre time for stability of the disc or starburst and the local cloud freefall time (see KDM12 for details[1]). In this way, the MW clouds and the extragalactic data seem to exhibit a much tighter correlation, which is shown in Figure 2(a). KDM12 only included the C2D+GB clouds from H10 and the L10 clouds at the two different extinction thresholds, while here we add all data from H10, Wu et al. (2010, hereafter W10), and the clouds observed in Gutermuth et al. (2011, hereafter G11). We also include an average of the 200 pc resolution data ($A = 4.5 \times 10^4\,\mathrm{pc}^2$; A. Bolatto, private communication) of the Small Magellanic Cloud (SMC) (Bolatto et al. 2011). One might question whether mixing resolved measurements of MW clouds and galactic discs with unresolved discs and starbursts (KDM12) in a single plot produces a physically meaningful comparison, because of extinction and telescope resolution issues (e.g. Calzetti et al. 2012; Shetty et al. 2013). Encouragingly, however, we find in tests with synthetic observations at different extinction thresholds and telescope resolutions varying by a factor of 32 that measurements presented in the form of Figure 2 vary by less than a factor of two for fixed physical conditions (Appendix B).

The dashed line in Figure 2(a) shows the empirical relation by KDM12,

$$\Sigma_{\mathrm{SFR}} = \epsilon_{\mathrm{SF},0} \times \Sigma_{\mathrm{gas}}/t_{\mathrm{ff}}, \qquad (2)$$

with a constant proportionality factor, $\epsilon_{\mathrm{SF},0} = 1\%$, which we define here as the total star formation efficiency, $\epsilon_{\mathrm{SF},0} \equiv \epsilon \times \mathrm{SFE}$. In this expression for $\epsilon_{\mathrm{SF},0}$, the *local* core-to-star efficiency, $\epsilon = 0.3$–0.7, is the fraction of infalling gas that is accreted by the star (Matzner & McKee 2000), i.e. about half. The other half is expelled by jets, winds and outflows. The *global* (cloud-scale) efficiency, $\mathrm{SFE} = 1\%$–6%, is the typical fraction of gas forming stars in a whole molecular cloud (Evans et al. 2009; Lada et al. 2010; Federrath & Klessen 2013). This yields a combined, total star formation efficiency, $\epsilon_{\mathrm{SF},0} \sim 0.3\%$–4.2%. Here we adopt an intermediate value, $\epsilon_{\mathrm{SF},0} = 1\%$, as favoured in observations and analytic models (Krumholz & Tan 2007; Renaud et al. 2012); however, we also study the influence of varying $\epsilon_{\mathrm{SF},0}$ below. The observational data in Figure 2(a) indeed exhibit a better correlation than in Figure 1, yet the scatter is still significant and remained largely unexplained in KDM12. What is the origin of this persistent scatter?

To advance on this issue, we compare the observations with computer simulations from Federrath & Klessen (2012, hereafter FK12), covering a substantial range of observed physical cloud parameters with Mach numbers $\mathcal{M} = \sigma_v/c_{\mathrm{s}} = 5$–50, different driving of the turbulence parametrized by $b = 1/3$ for solenoidal (divergence-free), $b = 0.4$ for mixed and $b = 1$ for compressive (rotation-free) driving, as well as a few different magnetic field strengths

---

[1] The high-z disc and starburst galaxy dataset in table 4 of KDM12 contains errors related to the computation of the Toomre time [M. Krumholz, private communication]. Figure 2 here shows the corrected data.
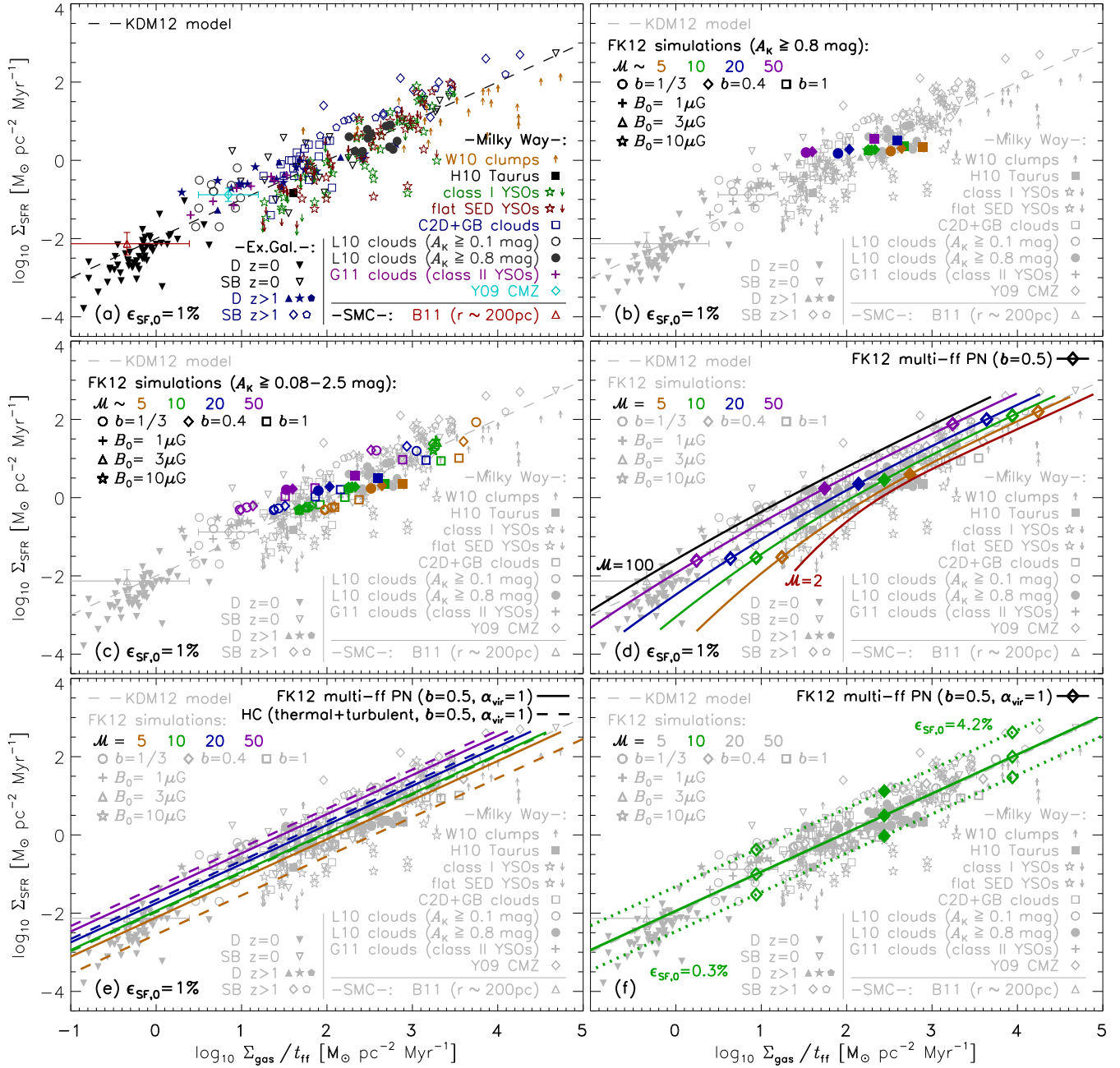
Figure 2. **(a)**: Same as Figure 1, but showing Σ_{SFR} as a function of Σ_{gas}/t_{ff}. Equation (2) with $\epsilon_{SF,0} = 1\%$ suggested by KDM12 is shown as the dashed line. Observational uncertainties (see Figure 1 caption) are higher in this representation, because of the additional uncertainties in t_{ff} (see Appendix A). **(b)**: Same as (a), but with simulations from FK12 (Federrath & Klessen 2012) evaluated for $\epsilon_{SF,0} = 1\%$ and $A_K \geqslant 0.8$ mag superposed. These are hydrodynamic computer models with turbulent Mach number $\mathcal{M} \sim 5$ (orange), 10 (green), 20 (blue), and 50 (purple), respectively, for solenoidal ($b = 1/3$; circles), mixed ($b = 0.4$; diamonds), and compressive driving ($b = 1$; squares) of the turbulence. Magnetohydrodynamic simulations with $\mathcal{M} \sim 10$, $b = 0.4$, and typical magnetic fields, $B_0 = 1$, 3, and $10\,\mu$G (cross, triangle, and star) are also shown, but these magnetized models are almost indistinguishable from the $B = 0$ models. **(c)**: Same as (b), but the simulations were not only evaluated at $A_K \geqslant 0.8$ mag (filled symbols), but at a range of extinction thresholds, $A_K \geqslant 0.08$–2.5 mag (open symbols). **(d)**: Same as (c), but with theoretical model curves given by Equations (3) and (4) superposed for a typical turbulent driving parameter $b = 0.5$ and $\mathcal{M} = 2$, 5, 10, 20, 50, and 100, each evaluated at different densities (equivalent to a range of extinction thresholds, to cover the range of observational Σ_{gas}/t_{ff}). **(e)**: Same as (d), but enforcing a virial parameter $\alpha_{vir} = 1$ in Equation (4) and additionally showing the Hennebelle & Chabrier (2011) (HC) version of our model for ϵ_{SF} as the dashed lines. **(f)**: Same as (e), but showing the effect of varying the efficiency $\epsilon_{SF,0} = 0.3\%$–4.2% in Equation (4) for fixed $\mathcal{M} = 10$.

with $B = 1$, 3 and $10 \, \mu\mathrm{G}$ for $\mathcal{M} = 10$ cases. In Figure 2(b), we superpose these computer simulations, measured at a fixed extinction threshold, $A_\mathrm{K} \geqslant 0.8 \, \mathrm{mag}$ and for $\epsilon_{\mathrm{SF},0} = 1\%$. To do this, we first produce column density projections along each coordinate axis of the three-dimensional simulations, when SFE $= 2\%$ of the total cloud mass has been accreted by sink particles (Federrath et al. 2010a). Multiplying this by the core-to-star efficiency $\epsilon = 0.5$ yields the target $\epsilon_{\mathrm{SF},0} = 1\%$ as for the KMD12 model. We then measure Σ_{gas} in structures above a given A_K threshold in each projection and determine the amount of gas that formed sink particles, Σ_{SF}, in the corresponding A_K contour[2]. We take the total mass in gas and the total mass in sink particles above a given A_K threshold and divide both by the cloud area that is above that extinction threshold to measure Σ_{gas} and Σ_{SF}, respectively. Finally, we compute $\Sigma_{\mathrm{SFR}} = \Sigma_{\mathrm{SF}}/(2 \, \mathrm{Myr})$ for class II YSOs, routinely applied by observers (Evans et al. 2009; Heiderman et al. 2010; Lada et al. 2010), such that our procedure to place the simulation data in Figure 2(b) matches the observational method as closely as possible. Note that this procedure does not necessarily reflect the true rate of star formation in the simulations (studied in detail in FK12), but places the simulation data as they would be placed if processed by an observer, who does not have any information about the time evolution.

Figure 2(b) shows that the simulations are consistent with the observations and roughly agree with the L10 clouds measured at the same extinction threshold, $A_\mathrm{K} \geqslant 0.8 \, \mathrm{mag}$. Comparing the simulations with one another, we arrive at three conclusions. First, for a fixed Mach number, the simulations with compressive driving exhibit higher $\Sigma_{\mathrm{gas}}/t_{\mathrm{ff}}$ and Σ_{SFR} than the respective simulations with mixed and solenoidal driving. Secondly, $\Sigma_{\mathrm{gas}}/t_{\mathrm{ff}}$ decreases with increasing $\mathcal{M}$, while Σ_{SFR} stays almost constant. Thirdly, magnetic fields reduce $\Sigma_{\mathrm{gas}}/t_{\mathrm{ff}}$, but only very marginally.

Evaluating the same simulations as in Figure 2(b) not only at $A_\mathrm{K} \geqslant 0.8 \, \mathrm{mag}$, but at a range of extinction thresholds, $A_\mathrm{K} \geqslant 0.08$–$2.5 \, \mathrm{mag}$, we obtain the distribution of simulation data shown in Figure 2(c). We find that the roughly linear proportionality between Σ_{SFR} and $\Sigma_{\mathrm{gas}}/t_{\mathrm{ff}}$ is primarily driven by changes in the extinction value defining the clouds. This was already seen when we compared the L10 clouds at $A_\mathrm{K} \geqslant 0.1 \, \mathrm{mag}$ and $A_\mathrm{K} \geqslant 0.8 \, \mathrm{mag}$ in panel (a). The only difference is that the simulation data do not have the dynamic range (because of limited numerical resolution) to reach down to the very low extinction values in the L10 clouds.

Figure 2(c) confirms the effect of increasing sonic Mach number seen in panel (b), i.e. clouds with higher $\mathcal{M}$ shift to lower $\Sigma_{\mathrm{gas}}/t_{\mathrm{ff}}$. The reason for this is that Σ_{gas} is almost fixed for a given A_K threshold, but $1/t_{\mathrm{ff}} \propto \rho^{1/2} \propto \ell^{-1/2} \propto \mathcal{M}^{-1}$ varies with cloud size ℓ and Mach number (which is why clouds with Mach 50 have about $10\times$ lower $\Sigma_{\mathrm{gas}}/t_{\mathrm{ff}}$ than Mach 5 clouds in Figure 2b) as the simulations roughly follow the Larson (1981) relations for the velocity dispersion and density as a function of cloud size (see FK12, table 2). A substantial fraction of the observed scatter in $\Sigma_{\mathrm{gas}}/t_{\mathrm{ff}}$

may thus be explained by variations in the turbulent Mach number. If the clouds that form stars actually follow the Larson relations in the same way as the simulations do here, then we may relate the observational data directly to the simulation data. However, some regions do not follow the standard Larson relations (e.g. the Central Molecular Zone (CMZ); see Shetty et al. 2012, and potentially also extragalactic systems), such that those regions will probably not be consistent with the simulations. However, the scatter seen in the observations may still be attributable to variations in the Larson relations.

3   A THEORETICAL MODEL FOR Σ_{SFR}

To substantiate this finding, we add theoretical model curves in Figure 2(d). These models are based on the statistics of supersonic magnetohydrodynamic turbulence in self-gravitating systems (Krumholz & McKee 2005; Padoan & Nordlund 2011; Hennebelle & Chabrier 2011). Here we focus on the best-fitting multi-freefall PN model in FK12 and compute

$$\Sigma_{\mathrm{SFR}} = \epsilon_{\mathrm{SF}} \times \Sigma_{\mathrm{gas}}/t_{\mathrm{ff}}, \tag{3}$$

where $\Sigma_{\mathrm{gas}} = \rho\ell$, i.e. the product of gas density ρ and size ℓ of the cloud structure. Equation (3) is the same as Equation (2), but instead of a constant proportionality factor $\epsilon_{\mathrm{SF},0}$, we evaluate the dimensionless function

$$\epsilon_{\mathrm{SF}} = \frac{\epsilon_{\mathrm{SF},0}}{2\phi_t} \exp\left(\frac{3}{8}\sigma_s^2\right) \left[1 + \mathrm{erf}\left(\frac{\sigma_s^2 - s_{\mathrm{crit}}}{\sqrt{2\sigma_s^2}}\right)\right]. \tag{4}$$

Equation (4) is derived from an integral over the high-density tail of the log-normal probability distribution function (PDF) of the turbulent gas density (Vázquez-Semadeni 1994; Federrath et al. 2008)[3],

$$p(s) = \frac{1}{\sqrt{2\pi\sigma_s^2}} \exp\left(-\frac{(s - s_0)^2}{2\sigma_s^2}\right), \tag{5}$$

expressed in terms of the logarithmic density, $s \equiv \ln(\rho/\rho_0)$, where ρ_0 is the mean density and $s_0 = -0.5\,\sigma_s^2$ is the logarithmic mean density. This integral is weighted by ρ/ρ_0 to estimate the mass fraction of gas above a critical density s_{crit} and weighted by a freefall-time factor to construct a dimensionless SFR:

$$\epsilon_{\mathrm{SF}} = \frac{\epsilon_{\mathrm{SF},0}}{\phi_t} \int_{s_{\mathrm{crit}}}^{\infty} \frac{t_{\mathrm{ff}}(\rho_0)}{t_{\mathrm{ff}}(\rho)} \frac{\rho}{\rho_0} \, p(s)\mathrm{d}s. \tag{6}$$

Note that the factor $t_{\mathrm{ff}}(\rho_0)/t_{\mathrm{ff}}(\rho)$ is evaluated *inside* the integral because gas with different densities has different freefall times (Hennebelle & Chabrier 2011, 2013). The factor $\epsilon_{\mathrm{SF},0}$ is the same as in Equation (2), and $1/\phi_t$ (Krumholz

---

[2] We do not distinguish connected from disconnected structures. We simply take a column density threshold and sum up all the simulation pixels that are above a given A_K threshold.

[3] Although the PDF can develop a power-law tail when gas starts to collapse (Klessen 2000; Collins et al. 2012), a strong tail only occurs once SFE $\approx 5\%$ (Federrath & Klessen 2013), at which point star formation typically shuts off due to feedback processes. We thus conclude that a log-normal PDF is a reasonably good approximation for a simple theoretical model of the SFR, even when the density structure comes from a mixture of turbulence, gravitational instabilities, feedback, or cooling and heating processes (Wada & Norman 2001; Bournaud et al. 2010; Glover et al. 2010).

& McKee 2005) accounts for the uncertainty in the timescale factor, which was measured to $1/\phi_t \approx 0.5$ in FK12.

The variables σ_s and s_{crit} in Equation (4) are the standard deviation of the density PDF (Molina et al. 2012), $\sigma_s^2 = \ln\left[1 + b^2 \mathcal{M}^2 \beta/(\beta+1)\right]$, and the critical density (Padoan & Nordlund 2011), $s_{\mathrm{crit}} = \ln\left[0.067\theta^{-2}\alpha_{\mathrm{vir}}\mathcal{M}^2 f(\beta)\right]$ with $f(\beta) = (1+\beta^{-1})^{-2}(1+0.925\beta^{-3/2})^{2/3}$ and the virial parameter $\alpha_{\mathrm{vir}} = 5\sigma_v^2/(G\rho\ell^2)$ (Bertoldi & McKee 1992). The numerical factor $\theta \approx 1$ was measured in FK12 and physically motivated in Padoan & Nordlund (2011). Combining all this yields $\epsilon_{\mathrm{SF}} \equiv \epsilon_{\mathrm{SF}}(\alpha_{\mathrm{vir}}, \mathcal{M}, b, \beta)$, i.e. a dimensionless SFR as a function of four basic cloud parameters: α_{vir}, $\mathcal{M}$, the turbulent driving parameter $1/3 \leqslant b \leqslant 1$ (Federrath et al. 2008, 2010b), and the ratio of thermal to magnetic pressure, β.

Since we concluded from the simulations above that magnetic fields only have a relatively weak effect (with very strong magnetic fields, the SFR is reduced by a factor of 2–3, see Padoan & Nordlund 2011; Padoan et al. 2012, FK12), for simplicity we only consider theoretical cases without magnetic fields in the following ($\beta \to \infty$). Although there is no doubt that magnetic fields modify the picture, they are unlikely the primary controller of the order-of-magnitude variations that we see in the observations. For the same reason, we only consider a fixed, intermediate turbulent driving parameter $b = 0.5$ (Brunt 2010; Price et al. 2011; Kainulainen & Tan 2013; Kainulainen et al. 2013). We further use the total efficiency $\epsilon_{\mathrm{SF},0} = 1\%$ as before.

Figure 2(d) shows Equation (3) evaluated for four cloud sizes $\ell = 1$, 4, 16, and 100 pc. These correspond to $\mathcal{M} \sim 5$, 10, 20, and 50, according to the velocity dispersion–size relation (Larson 1981; Heyer & Brunt 2004), $\sigma_v = \mathcal{M}c_{\mathrm{s}} \approx 1\,\mathrm{km\,s}^{-1}(\ell/\mathrm{pc})^{0.5}$ with $c_{\mathrm{s}} \approx 0.2\,\mathrm{km\,s}^{-1}$, typical for molecular gas with temperatures of about 10 K and standard solar composition (Omukai et al. 2005). We also note in this context that Dib (2011) and Glover & Clark (2012) find that the SFR depends slightly on metallicity, introducing changes by a factor of 2–3, so the order-of-magnitude variations seen in observations cannot be explained by metallicity effects alone, but they may contribute.

In order to cover the range of A_{K} and $\Sigma_{\mathrm{gas}}/t_{\mathrm{ff}}$ in the observations, we vary the density along each theoretical model curve as a free parameter. Using the density–size relation (Larson 1981; Mac Low & Klessen 2004; McKee & Ostriker 2007) $\rho = \rho_0(\ell/\mathrm{pc})^{-1}$ with a typical density scale $\rho_0 = 10^4\mu_{\mathrm{H}}\,\mathrm{cm}^{-3}$ (where $\mu_{\mathrm{H}} = 1.67 \times 10^{-24}\,\mathrm{g}$ is the atomic mass of hydrogen), similar to the simulated clouds in Figure 2(b) and similar to the L10 clouds for $A_{\mathrm{K}} \geqslant 0.8\,\mathrm{mag}$, we obtain the filled diamonds in Figure 2(d), which agree well with the computer models for that extinction threshold. We also add the open diamonds, representing the same theoretical data, but for $10\times$ larger and smaller density scale ρ_0. For a given density scale, Σ_{SFR} is almost independent of $\mathcal{M}$, only $\Sigma_{\mathrm{gas}}/t_{\mathrm{ff}} \propto \mathcal{M}^{-1}$ for constant Σ_{gas} as we saw above for the simulation data. This implies that ϵ_{SF} in Equation (4) increases with $\mathcal{M}$ (because increasing $\mathcal{M}$ leads to stronger gas compression and thus higher relative SFRs, see FK12), effectively compensating the decrease of $\Sigma_{\mathrm{gas}}/t_{\mathrm{ff}}$ with $\mathcal{M}$. Indeed, $\epsilon_{\mathrm{SF}} \propto \mathcal{M}^{3/4}$ for $\mathcal{M} \gtrsim 10$ and $\alpha_{\mathrm{vir}} \sim 1$, leading to a weak dependence of $\Sigma_{\mathrm{SFR}} \propto \mathcal{M}^{-1/4}$ for fixed Σ_{gas}.

Changing the density scale ρ_0 in Figure 2(d) means that the virial parameter is about unity for the filled diamonds and about 0.1 and 10 for the open diamonds, respectively

to the right and to the left of the filled diamonds ($\alpha_{\mathrm{vir}} = 1$). Such a systematic correlation of α_{vir} with Σ_{SFR} is rather unexpected, which is why we add another panel (e) where we keep $\alpha_{\mathrm{vir}} = 1$ in Equation (4) along each model curve. Although variations in α_{vir} by at least two orders of magnitude are measured for MW clouds (Roman-Duval et al. 2010; Padoan & Nordlund 2011; Kauffmann et al. 2013) and certainly contribute to the scatter, the overall Mach number dependence remains, even if we enforce $\alpha_{\mathrm{vir}} = 1$.

Figure 2(e) additionally shows the Hennebelle & Chabrier (2011, 2013) (HC) version of our model for ϵ_{SF} with otherwise identical parameters and $y_{\mathrm{cut}} = 0.1$ (see FK12 for details of that model). The Mach number dependence is stronger, because the critical density in the HC model is $\rho_{\mathrm{crit}} \propto \mathcal{M}^{-2}$ unlike in the PN model, where $\rho_{\mathrm{crit}} \propto \mathcal{M}^2$ (see FK12, table 1). Both the multi-freefall PN and HC models support the basic idea that variations in the star formation relation may be caused by variations in the Mach number, but the details of that dependence are subject to significant uncertainties, introduced by the particular choice of model.

Finally, Figure 2(f) shows the effect of varying the efficiency $\epsilon_{\mathrm{SF},0} = 0.3\%$–$4.2\%$ in Equation (4) for fixed $\mathcal{M} = 10$, which covers a substantial fraction of the observed variations in Σ_{SFR}. Thus, for any point in the Σ_{SFR}–$\Sigma_{\mathrm{gas}}/t_{\mathrm{ff}}$ relation, there is a degeneracy between the Mach number and the efficiency, which can only be broken by measuring both $\mathcal{M}$ and $\epsilon_{\mathrm{SF},0}$ simultaneously.

4 DISCUSSION AND CONCLUSION

The main conclusion of this paper is that the observed scatter in the star formation law can be primarily explained by physical variations in the turbulent Mach number $\mathcal{M}$ and the star formation efficiency $\epsilon_{\mathrm{SF},0}$. We find that the observed scatter is not random, but instead depends systematically on $\mathcal{M}$ and $\epsilon_{\mathrm{SF},0}$. For a fixed extinction threshold or fixed Σ_{gas}, we find that $\Sigma_{\mathrm{gas}}/t_{\mathrm{ff}} \propto \mathcal{M}^{-1}$, if the standard Larson relations are in effect. Although some regions do not follow the standard Larson scalings (e.g. the CMZ and possibly extragalactic regions), we still expect a variation of $\Sigma_{\mathrm{gas}}/t_{\mathrm{ff}}$ also in such cases, albeit with a potentially different dependence. We further find that for fixed Σ_{gas}, the variations in Σ_{SFR} may be explained by variations in the star formation efficiency, systematically $\Sigma_{\mathrm{SFR}} \propto \epsilon_{\mathrm{SF},0}$ (see Figure 2f). The theoretical model, Equation (4), also implies that some fraction of the scatter may be explained by variations in the virial parameter α_{vir}, the turbulent driving parameter b, and the thermal-to-magnetic pressure ratio β.

We note that Renaud et al. (2012) have also recently developed an analytic model for Σ_{SFR} based on the log-normal density PDF and investigated the Mach number dependence of their model in the context of Kennicutt-Schmidt relations, such as plotted in Figure 1. They use Mach numbers in the range 1–20, gas scale heights of 5–2000 pc and density thresholds of 10–100 cm^{-3} to explain observations of MW clouds, discs and starbursts. The relatively low Mach numbers come about, because they chose to evaluate $\mathcal{M}$ for temperatures of the warm interstellar medium ($T \approx 10^{3-4}\,\mathrm{K}$). It is, however, the cold, molecular phase with $T \approx 10^{1-2}\,\mathrm{K}$ (where a log-normal PDF seems reasonable; see Glover et al. 2010) in which stars form, so the relevant Mach numbers for

the star-forming gas are about an order of magnitude higher than assumed in Renaud et al. (2012), because $\mathcal{M} \propto T^{-1/2}$.

Our simulations and theoretical models in Figure 2 make direct predictions that can be tested with observations. If the Mach number and star formation efficiency were indeed the primary physical reasons for the variations in the star formation relation, then measuring $\mathcal{M}$ and $\epsilon_{\mathrm{SF},0}$ in clouds and galaxies will eventually enable us to test these predictions. For example, the clouds and YSO data in the MW are in the expected range, $\mathcal{M} \sim 2$–20 and $\epsilon_{\mathrm{SF},0} \sim 0.3\%$–4.2%, consistent with our theoretical models. The placement of the CMZ is also consistent with $\mathcal{M} \sim 50$, given the uncertainties in the data. However, measurements of $\mathcal{M}$ and $\epsilon_{\mathrm{SF},0}$ in extragalactic systems are more difficult. For Arp 220, $\mathcal{M} \approx 100$ with large uncertainties (Downes & Solomon 1998). Arp 220 (the rightmost downward pointing triangle in Figure 2(a)[4]) would be more consistent with $\mathcal{M} \sim 10$ for $\epsilon_{\mathrm{SF},0} = 1\%$, which means that either our model is incorrect or $\epsilon_{\mathrm{SF},0}$ is relatively small for that galaxy, or the measurements of $\mathcal{M}$, Σ_{SFR}, Σ_{gas} and t_{ff} are so uncertain for Arp 220 that it cannot be used to falsify the model, or the standard Larson relations do not apply for Arp 220, such that a direct matching of Mach numbers there and in our models (that assume standard Larson scaling) cannot be done with the present data. Finally, the SMC has velocity dispersions of 10–40 km s^{-1} (Bekki & Chiba 2009), which gives $\mathcal{M} = 16$–200 for $T = 10$–100 K, basically consistent with our theoretical model in Figure 2, but also with large uncertainties, so we need future observations that simultaneously constrain $\mathcal{M}$ and $\epsilon_{\mathrm{SF},0}$.

APPENDIX A: CAVEATS AND LIMITATIONS

Here we discuss caveats and limitations of the present study. First, unlike the classical Kennicutt-Schmidt relation, which only requires measurements of column-integrated quantities, Σ_{SFR} and Σ_{gas}, the KDM12 model requires an additional estimate of the volume density ρ to compute the freefall time for the abscissa $\Sigma_{\mathrm{gas}}/t_{\mathrm{ff}}$. The current estimate of ρ by KDM12 assumes that the gas is homogeneously distributed along the line of sight (LOS). This is clearly an oversimplification, because the gas along the LOS has likely a range of densities and potentially contributions from different cloud

---

[4] The starburst galaxy Arp 220 is erroneously listed as 'NGC 6946' in KDM12, because of a mismatch of the original K98 tables and the KDM12 table for disc and starburst galaxies. An erratum of KDM12 is in preparation (M. Krumholz, private communication). A corrected table is available upon request.
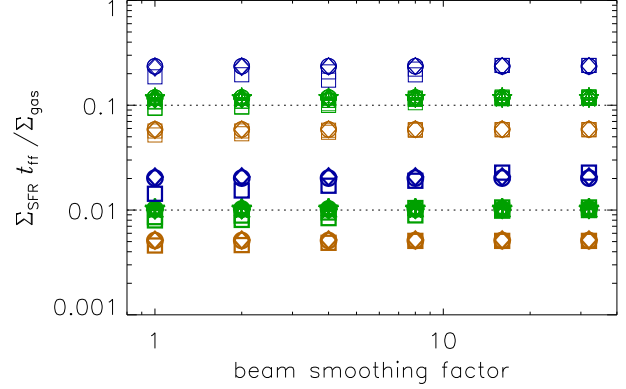

Figure B1. $\epsilon_{\mathrm{SF}} = \Sigma_{\mathrm{SFR}} t_{\mathrm{ff}}/\Sigma_{\mathrm{gas}}$ as a function of beam smoothing factor for $\epsilon_{\mathrm{SF},0} = 1\%$ (lower set) and $\epsilon_{\mathrm{SF},0} = 10\%$ (upper set). Varying the telescope resolution merely shifts the data along the star formation law, $\epsilon_{\mathrm{SF}} = \mathrm{const}$ (shown as the dotted lines for $\epsilon_{\mathrm{SF},0} = 1\%$ and 10% for $\mathcal{M} = 10$ simulations; green symbols). Simulation symbols and colours are the same as in Figure 2(b) and (c).

components in the case of very long LOS. Eventually, a refined model would take the multi-freefall contributions of the PDF of gas densities along the LOS into account. Secondly, most of the MW cloud and YSO data use a fixed star formation time scale of 2 Myr for the class II phase (Evans et al. 2009; Heiderman et al. 2010; Lada et al. 2010) to estimate Σ_{SFR}. However, the exact value of Σ_{SFR} depends on the evolutionary phase and requires information about the time evolution of the cloud, which is not available from observations. Thus, estimates of Σ_{SFR} are highly uncertain and some spread of the data is likely caused by this effect (for effects of different star formation timescales, see Federrath & Klessen 2012).

APPENDIX B: EFFECTS OF THE TELESCOPE RESOLUTION

Figure B1 shows the influence of the telescope resolution. We made synthetic observations of the simulations as in Figure 2(b), but with up to $32\times$ beam smoothing ($32\times$ reduced telescope resolution or observing the same cloud at a $32\times$ greater distance). Although Σ_{SFR} and $\Sigma_{\mathrm{gas}}/t_{\mathrm{ff}}$ are both reduced by beam smoothing, they are reduced by roughly the same factor, such that ϵ_{SF} is almost independent of telescope resolution. This result is encouraging for observations, because it shows that ϵ_{SF} could be measured even with relatively low resolution.

REFERENCES

Bekki, K., & Chiba, M. 2009, PASA, 26, 48
Bertoldi, F., & McKee, C. F. 1992, ApJ, 395, 140
Bigiel, F., Leroy, A., Walter, F., et al. 2008, AJ, 136, 2846
Bolatto, A. D., Leroy, A. K., Jameson, K., et al. 2011, ApJ, 741, 12
Bouché, N., Cresci, G., Davies, R., et al. 2007, ApJ, 671, 303

Bournaud, F., Elmegreen, B. G., Teyssier, R., Block, D. L., & Puerari, I. 2010, MNRAS, 409, 1088

Brunt, C. M. 2010, A&A, 513, A67

Calzetti, D., Liu, G., & Koda, J. 2012, ApJ, 752, 98

Collins, D. C., Kritsuk, A. G., Padoan, P., et al. 2012, ApJ, 750, 13

Daddi, E., Elbaz, D., Walter, F., et al. 2010, ApJ, 714, L118

Dib, S. 2011, ApJ, 737, L20

Downes, D., & Solomon, P. M. 1998, ApJ, 507, 615

Elmegreen, B. G. 2002, ApJ, 577, 206

Elmegreen, B. G., & Scalo, J. 2004, ARAA, 42, 211

Evans, II, N. J., Dunham, M. M., Jørgensen, J. K., et al. 2009, ApJ, 181, 321

Federrath, C., Banerjee, R., Clark, P. C., & Klessen, R. S. 2010a, ApJ, 713, 269

Federrath, C., & Klessen, R. S. 2012, ApJ, 761, 156 (FK12)

—. 2013, ApJ, 763, 51

Federrath, C., Klessen, R. S., & Schmidt, W. 2008, ApJ, 688, L79

Federrath, C., Roman-Duval, J., Klessen, R. S., Schmidt, W., & Mac Low, M. 2010b, A&A, 512, A81

Ferrière, K. M. 2001, RvMP, 73, 1031

Genzel, R., Tacconi, L. J., Gracia-Carpio, J., et al. 2010, MNRAS, 407, 2091

Glover, S. C. O., & Clark, P. C. 2012, MNRAS, 426, 377

Glover, S. C. O., Federrath, C., Mac Low, M., & Klessen, R. S. 2010, MNRAS, 404, 2

Gutermuth, R. A., Pipher, J. L., Megeath, S. T., et al. 2011, ApJ, 739, 84 (G11)

Heiderman, A., Evans, II, N. J., Allen, L. E., Huard, T., & Heyer, M. 2010, ApJ, 723, 1019 (H10)

Hennebelle, P., & Chabrier, G. 2011, ApJ, 743, L29 (HC)

—. 2013, ApJ, 770, 150

Heyer, M. H., & Brunt, C. M. 2004, ApJ, 615, L45

Kainulainen, J., Federrath, C., & Henning, T. 2013, A&A, 553, L8

Kainulainen, J., & Tan, J. C. 2013, A&A, 549, A53

Kauffmann, J., Pillai, T., & Goldsmith, P. F. 2013, ApJ, in press (arXiv:1308.5679)

Kennicutt, Jr., R. C. 1998, ApJ, 498, 541

Klessen, R. S. 2000, ApJ, 535, 869

Krumholz, M. R., Dekel, A., & McKee, C. F. 2012, ApJ, 745, 69 (KDM12)

Krumholz, M. R., & McKee, C. F. 2005, ApJ, 630, 250

Krumholz, M. R., & Tan, J. C. 2007, ApJ, 654, 304

Lada, C. J., Lombardi, M., & Alves, J. F. 2010, ApJ, 724, 687 (L10)

Larson, R. B. 1981, MNRAS, 194, 809

Mac Low, M.-M., & Klessen, R. S. 2004, RvMP, 76, 125

Matzner, C. D., & McKee, C. F. 2000, ApJ, 545, 364

McKee, C. F., & Ostriker, E. C. 2007, ARAA, 45, 565

Molina, F. Z., Glover, S. C. O., Federrath, C., & Klessen, R. S. 2012, MNRAS, 423, 2680

Omukai, K., Tsuribe, T., Schneider, R., & Ferrara, A. 2005, ApJ, 626, 627

Padoan, P., Haugbølle, T., & Nordlund, Å. 2012, ApJ, 759, L27

Padoan, P., & Nordlund, Å. 2011, ApJ, 730, 40 (PN)

Price, D. J., Federrath, C., & Brunt, C. M. 2011, ApJ, 727, L21

Renaud, F., Kraljic, K., & Bournaud, F. 2012, ApJ, 760, L16

Roman-Duval, J., Jackson, J. M., Heyer, M., Rathborne, J., & Simon, R. 2010, ApJ, 723, 492

Schmidt, M. 1959, ApJ, 129, 243

Shetty, R., Beaumont, C. N., Burton, M. G., Kelly, B. C., & Klessen, R. S. 2012, MNRAS, 425, 720

Shetty, R., Kelly, B. C., & Bigiel, F. 2013, MNRAS, 430, 288

Stahler, S. W., & Palla, F. 2004, The formation of stars (Weinheim: Wiley-VCH)

Tacconi, L. J., Genzel, R., Neri, R., et al. 2010, Nature, 463, 781

Vázquez-Semadeni, E. 1994, ApJ, 423, 681

Wada, K., & Norman, C. A. 2001, ApJ, 547, 172

Wu, J., Evans, II, N. J., Shirley, Y. L., & Knez, C. 2010, ApJ, 188, 313 (W10)

Yusef-Zadeh, F., Hewitt, J. W., Arendt, R. G., et al. 2009, ApJ, 702, 178